RSC Advances

PAPER

View Article Online
View Journal | View Issue

Cite this: *RSC Adv.*, 2025, **15**, 37645

pH-responsive doxorubicin-loaded *Artemisia argyi* carbon dots: enhanced targeted therapy for hepatocellular carcinoma

Ruilong Jia,† Ping Liu,† Yanli Gong, Yuting Gao, Yajun Xiong, Xiaoyong Song, Jinglin Peng, Meiqi Lan and Xinli Shi *

Hepatocellular carcinoma (HCC), a lethal form of liver cancer within the gastrointestinal tract, demonstrates dismal survival rates and challenging treatment prospects. Doxorubicin (DOX) continues to be extensively employed as a chemotherapeutic drug for hepatocellular carcinoma in clinical practice. Nevertheless, its lack of selective targeting leads to non-specific killing of normal healthy cells, thereby inducing severe adverse reactions. Carbon dots (CDs) with biocompatibility and low toxicity have attracted much attention in cancer treatment. We demonstrate an eco-friendly and straightforward synthesis of CDs with superior biocompatibility *via* a hydrothermal method, utilizing *Artemisia argyi* as the carbon precursor, and doxorubicin-loaded carbon dots (CDs–DOX) provide a novel strategy for liver cancer treatment. Compared with DOX, CDs–DOX showed more significant anti-tumor advantages. CDs–DOX enhanced the relative abundance of *A. muciniphila* in the intestinal microbiota, reshape the homeostasis of intestinal flora in mice, and significantly enhance the intestinal barrier function. The antitumor effects of CDs–DOX against HCC involve regulation of pivotal genes and alteration of the tumor microenvironment. In addition, CDs–DOX significantly reduce DOX heart and liver toxicity, reduce treatment-related adverse reactions, and provide a safer and more efficient new strategy for combined treatment of tumors.

Received 5th August 2025
Accepted 1st October 2025

DOI: 10.1039/d5ra05688h

rsc.li/rsc-advances

1 Introduction

Hepatocellular carcinoma (HCC) demonstrates a prevalence ranking of sixth among all cancers and accounts for the third highest mortality rate worldwide. During 2022, malignant tumors affected 19.97 million individuals globally while claiming 9.74 million lives. Approximately 865 000 new cases of hepatocellular carcinoma were estimated to occur globally each year, along with 758 000 attributable deaths.[1] The early treatment of HCC is surgical resection and liver transplantation,[2] which may lead to a higher risk of recurrence and metastasis.[3] Chemotherapeutic approaches have constituted a mainstay of cancer treatment for about 100 years, retaining widespread clinical application and effectiveness.[4] Evidence confirms that combining chemotherapy with surgical intervention and radiation therapy enhances progression-free survival in localized cancer cases.[5] Although a lot of research has been invested in cancer, drug resistance is still the most serious factor hindering effective treatment. Consequently, the development of novel, efficient therapeutic approaches for HCC constitutes an immediate research imperative.[6] Doxorubicin (DOX), a widely utilized chemotherapeutic drug with broad-spectrum antitumor activity, plays a significant role in HCC management. DOX remains the most widely utilized anthracycline anticancer drug.[7] Anthracycline drugs have always been an important and effective treatment for a variety of cancers. However, the clinical application of these agents is challenged by severe adverse effects and toxicity.[8] Hence, a major scientific challenge lies in developing methods to alleviate DOX-related side effects and improve its clinical utility.

To achieve this, researchers have developed many targeted drug delivery systems using carriers including polymers, liposomes, microspheres, and carbon dots. Carbon dots (CDs) have emerged as a promising category of carbon-based nanocarriers in drug delivery applications, distinguished by their exceptional biocompatibility, minimal cytotoxicity, excellent aqueous dispersibility, and remarkable optical characteristics.[9] The unique properties of CDs enable their utilization in several cutting-edge research areas, particularly in fluorescence imaging, biological detection, nanomedicine, and light-driven catalytic reactions. On this foundation, CDs synthesized with biologically active constituents serving as precursor materials were developed for biomedical applications. The donkey-hide gelatin-based carbon nanomaterials exhibit potent erythropoiesis-promoting capabilities by enhancing hematopoietic progenitor cell proliferation, inducing erythroid differentiation, promoting erythroblast

Laboratory of Integrated Medicine Tumor Immunology, Shanxi University of Chinese Medicine, Taiyuan, 030000, China. E-mail: sxlsunshine@sina.com
† Ruilong Jia and Ping Liu contributed equally to this work.

maturation, and systematically activating the entire erythrocyte production cascade.[10] Carbon dots synthesized from honeysuckle exhibit dual catalytic and pharmacological properties that attenuate pulmonary inflammation through suppression of the caspase-11/gasdermin D-mediated pyroptotic pathway.[11] Among the numerous biomass materials, Chinese herbal medicine hold more promise as active precursors for synthesizing CDs due to their abundant active components and long history of clinical application. Notably, Chinese herbal medicine possesses a distinct advantage over Western pharmaceuticals in its diverse array of bioactive components, offering multi-target therapeutic potential.[12] *Artemisia argyi* is a medicinal and edible Chinese herbal medicine, which has antibacterial and antiviral effects.[13] Therefore, CDs made from *Artemisia argyi* may have certain antibacterial, antiviral and anti-inflammatory effects.

This study utilized *Artemisia argy*i as a natural precursor material to fabricate CDs, with DOX being incorporated as a model chemotherapeutic to assess drug delivery enhancement strategies for improved cancer treatment outcomes. The study involved systematic evaluation of CDs properties through physicochemical analyses and subsequent determination of doxorubicin loading efficiency and release kinetics using carbon nanospheres. In animal experiments, we constructed a subcutaneous xenograft model of Hepa1-6 and found that CDs–DOX had tumor-targeted delivery and improved tumor malignancy compared with free DOX. Notably, CDs–DOX stimulated proliferation of *A. muciniphila*, a beneficial mucinolytic gut microbe, demonstrating its capacity to concurrently restrain tumor development and favorably influence mouse intestinal microflora. Transcriptome sequencing showed that CDs–DOX had significant systemic immunomodulatory effects. In addition, compared with DOX, HE staining of liver, heart, spleen, lung and kidney showed that the heart and liver toxicity of CDs–DOX was significantly reduced. In summary, CDs–DOX represents a potential approach to enhance the therapeutic outcome for hepatocellular carcinoma (HCC), thus providing new insights for anticancer therapy (Scheme 1).

2 Materials and methods

2.1. Material

Artemisia argyi in this experiment was obtained from Yangquan City, Shanxi Province. DOX was sourced from Shanghai Baililai Biotechnology (Chengdu, China). All experimental materials – PBS, syringe filters, and 1 kDa cutoff dialysis membranes – were commercially acquired from Sigma-Aldrich.

2.2. Characterization

Sample microstructure was analyzed by transmission electron microscopy (JEM-2100F, JEOL Ltd, Japan) at 200 kV accelerating voltage. X-ray diffraction analysis was performed on the CDs with a Rigaku SmartLab 9 kW diffractometer to determine their crystallographic properties. FT-IR spectral data were collected using a Nicolet 6700 instrument (Thermo Fisher Scientific) with a scanning range of 400–4000 cm^{-1}. A Thermo Scientific ESCALAB 250Xi XPS instrument was employed for surface chemical analysis. A UV-2600 system was employed for absorption spectroscopy, while fluorescence measurements were conducted on an RF-6000 instrument (Japan).

2.3. Preparation of CDs

CDs were prepared *via* a hydrothermal approach using *Artemisia argyi* as raw material. The detailed procedure was conducted as follows: Dried and cleaned *Artemisia argyi* was ground with a crusher for 5 minutes to obtain moxa floss. Subsequently, 0.7 g of the prepared moxa floss was blended with 20 mL of distilled water. The resulting solution was transferred into the inner core of a hydrothermal reactor and subjected to ultrasonic oscillation at 37 °C for 10 minutes. Following sonication, the inner core containing the solution was placed into the hydrothermal reactor, which was then maintained at 200 °C in an oven for 3 h. Upon reaching room temperature *via* natural cooling, the mixture was centrifuged at 10 000 rpm for 15 min, and the clarified supernatant was filtered through 0.22 μm membranes. Following filtration, CDs were obtained through vacuum drying (100 °C, 8 h) of the processed solution.

2.4. DOX-loading and release

The drug carrying capacity of CDs was evaluated, according to the mass ratio of DOX to CDs of 2 : 1, 10 mg DOX and 5 mg CDs were respectively weighed and added into neutral PBS solutions with different volumes to prepare mixed solutions with different concentrations; the mixed solution was stirred at 37 °C and 600 rpm for 1 hour, the mixtures were kept in a 4 °C fridge for 12 h. After full loading, the mixed solution was centrifuged at 4000 rpm for 10 min; the precipitate in the centrifuge tube was repeatedly centrifuged and washed with neutral PBS solution until the UV-Vis absorption spectrum of the supernatant had no absorption peak at 490 nm, all the washing liquids were collected and the absorbance of the mixed washing liquid at 490 nm was determined; the absorbance of mixed solution was substituted into the standard curve, and then the mass $m_{DOX\text{-}loaded}$ of unloaded DOX was obtained according to the total volume of mixed washing solution; and the loading efficiency (DL) and encapsulation efficiency (EE) of CDs can be obtained according to the following formula.

$$DL = \frac{m_{DOX\text{-}loaded}}{m_{DOX\text{-}loaded} + m_{CDs}} \times 100\% \quad (1)$$

$$EE = \frac{m_{DOX\text{-}loaded}}{m_{DOX}} \times 100\% \quad (2)$$

2.5. Drug release

The optimal drug loading conditions (the mass ratio of CDs to DOX is 1 : 2, and the concentration of DOX is 0.7 mg mL^{-1})for drug release testing, CDs–DOX was dispersed in 100 mL PBS solutions with pH values of 4.0, 6.0 and 7.4 respectively, these conditions were established to simulate three biologically distinct environments: physiological milieu, interstitial fluid of

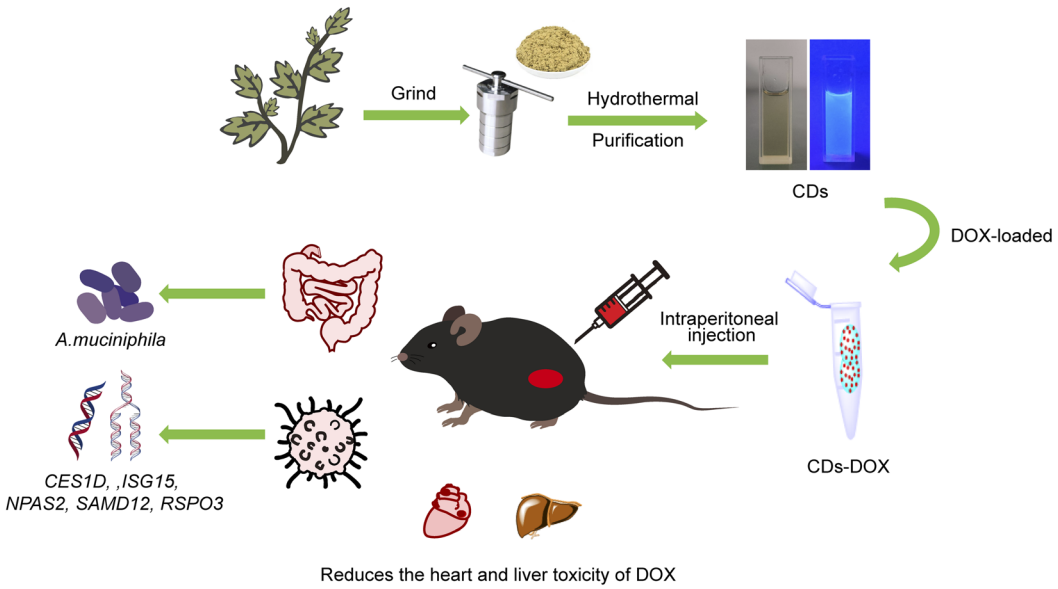

Scheme 1 Schematic illustration of the fabrication process for CDs–DOX and their application in hepatocellular carcinoma (HCC) therapy.

tumor tissues, and cytoplasm of cancer cells, the dispersion was loaded into a 1 kDa dialysis bag and immersed in PBS solutions with three different pH values for the drug release assay; at regular intervals, an appropriate amount of PBS solution was sucked to determine its absorbance at the wavelength of 490 nm until the PBS solution almost did not contained DOX, the drug release rate (DR) at each time interval was determined using the following eqn (3).

$$\mathrm{DR} = \frac{m_{\text{DOX-released}}}{m_{\text{DOX-loaded}}} \times 100\% \quad (3)$$

2.6. Animal experiments

Animal procedures were carried out following approval from the Institutional Animal Ethics Committee at Shanxi University of Traditional Chinese Medicine (registered number: AWE202403287). The laboratory animal quality certificate was provided by SPF (Beijing) Biotechnology Co., Ltd (license number: SCXK (Beijing) 2024-0001). Male C57BL/6 mice, 4 weeks old, grew in a controlled environment without specific pathogen (SPF) conditions. Animals were housed under controlled conditions (22–24 °C) with a 12 h light/12 h dark photoperiod.

2.7. Establishment and grouping of Hepa1-6 mouse subcutaneous tumor xenograft model

Five-week-old male C57BL/6 mice received subcutaneous implantation of 1×10^7 Hepa1-6 cells in the right hind limb. Tumor growth was quantified by the ellipsoid volume formula $V = (L \times W^2)/2$. After one week of tumor growth (50–100 mm^3), the mice were randomly assigned to six groups, as follows: PBS (090501, China), CDs (6.3 mg kg^{-1}), CDs–DOX-L (4.65 mg kg^{-1}), CDs–DOX-M (9.3 mg kg^{-1}), CDs–DOX-H (18.6 mg kg^{-1}) and DOX (5.31 mg kg^{-1}) (D807083, China), eight mice in each group. Treatment was administered *via* intraperitoneal route in three doses with 3 days inter-dose intervals. Tumor dimensions and weights were recorded every two days to evaluate growth kinetics. Standardized necropsy procedures were performed after cervical dislocation, with harvest of cardiac, hepatic, splenic, pulmonary, renal, colonic, and tumor tissues, all fixed in 4% PFA for histological processing (BL539A, China). Samples were stained with H&E (BA4098, China) and immunohistochemistry (PV-9000, China).

2.8. H&E staining

Following paraffin embedding, multiple organ tissues including liver, heart, spleen, lungs, kidneys and tumor nodules were precisely sectioned into 4-micron slices using computer-controlled rotary microtomy (Leica RM2265 Germany). Tissue sections underwent hematoxylin and eosin staining using a H&E kit, followed by microscopic examination and digital image acquisition to document histomorphological alterations (Leica DM4B, Germany).[14]

2.9. Immunohistochemistry (IHC)

Initially, antigen retrieval of the liver tissue sections was performed *via* high-pressure repair. Subsequently, the protocol described in the IHC kit was implemented. After incubation with primary antibody, secondary antibody and DAB color development kit (ZLI-9018, China) were added in turn for color reaction. Microscopic images of the sections were acquired using a microscope. The primary antibodies included Ki-67 (12202S, CST, USA, 1 : 200), Z0-1 (ab276131, Abcam, UK, 1 : 250), Occludin (27260-1-AP, Proteintech, China, 1 : 1000).

2.10. Periodic acid-schiff staining (PAS)

After tissue collection, murine colon samples were processed into paraffin sections and stained for goblet cells employing a PAS staining kit (R20526, China). Standardized staining protocols provided with the commercial kit were rigorously implemented. Post-staining microscopic analysis enabled systematic assessment of goblet cell density and cytomorphological changes in the intestinal epithelium of colon and ileum specimens (Leica DM2500, Germany), and images were collected for analysis to evaluate the secretory function and barrier function of intestinal mucosa.

2.11. Real – time PCR

Genomic DNA was extracted from murine fecal samples employing a commercial DNA isolation kit (EX1752, China), with subsequent quantification performed using a NanoDrop spectrophotometric system (USA). For the real-time PCR setup, DNA, double-distilled water (ddH_2O), forward, and SuperReal PreMIX Plus (WO229, China) were added to an 8-tube strip reaction system, followed by quantitative analysis using a Bio-Rad real-time PCR detection system (USA). The *A. muciniphila* primers used were AM1 (5′-CAGCACGTGAAGGTGGGAC-3′) and AM2 (5′-CCTTGCGGTTGGCTTCAGAT-3′). Quantitative data were analyzed *via* the $2^{-\Delta\Delta CT}$ algorithm. Primer sequences for total bacteria and *A. muciniphila* were adapted from previously published studies.[15]

2.12. 16 s rRNA sequencing

After 7 days of intervention, the feces of each group of mice were collected. Shanghai Pasenuo Biotechnology Co., Ltd was commissioned to sequence and analyze the microbial diversity of mouse feces. Microbial community analysis was conducted using the Gene Cloud platform to assess α-diversity indices and intergroup taxonomic variations, with graphical representations generated to illustrate gut microbiota composition across treatment cohorts.

2.13. Transcriptome sequencing

After the experiment was concluded, the tumor tissues were promptly removed. In accordance with the requirements, the tumor tissue samples from each group were sent to Shanghai Personal Biotechnology Co., Ltd. The company carried out procedures such as RNA extraction and library construction on the samples, followed by transcriptome sequencing. Subsequently, differential gene expression analysis, enrichment analysis, and clustering analysis were performed on the samples. These analyses were aimed at gaining in-depth insights into the changes in the gene expression profiles of tumor tissues after PBS and CDs–DOX-L treatment, and at exploring the underlying molecular mechanisms.

2.14. AST, ALT, BUN, CRE detection

The serum and plasma of mice were extracted for AST (C010-2-1, China), ALT (C009-2-1, China), BUN (C013-2-1, China), CRE (C013-2-1, China) detection. According to the instructions of the kit, the 96-well microplate was loaded with three sample types: standard references, blank controls, and experimental serum samples. The enzymatic activities of AST and ALT, along with serum concentrations of BUN and CRE, were quantified using standardized computational algorithms by using the enzyme calibration to measure the OD value at the specified nanometers.

2.15. Statistical analysis

Statistical evaluations were conducted employing GraphPad Prism 9.0 software. One-way ANOVA followed by Tukey's multiple comparison test was used for multigroup analyses. Quantitative data are shown as mean ± SD, with *p*-values below 0.05 considered significant.

3 Experimental result

3.1. Preparation and characterization of CDs and CDs–DOX

In the experiments, a simple hydrothermal approach was used to CDs from *Artemisia argyi.* TEM characterization revealed monodisperse CDs with near-spherical nanostructures, exhibiting a narrow size distribution centered at 2 nm (Fig. 1A and B). Such an ultrasmall size means that CDs could be well absorbed and metabolized by living organisms. The HRTEM analysis clearly demonstrated the presence of well-defined crystalline structures in CDs, exhibiting a lattice spacing of 0.51 nm (Fig. 1C). The XRD further revealed that CDs exhibited a broad peak at 24°, which was ascribed to the (002) plane of the graphite structure (Fig. 1D). The FT-IR profile in Fig. 1E displayed characteristic vibrational modes of CDs, where the prominent absorption band centered at 3335 cm^{-1} was indicative of the stretching vibrations of O–H and N–H groups. The absorption peak at 2950 cm^{-1} corresponds to C–H bond stretching vibrations. The characteristic bands observed at 1673 and 1400 cm^{-1} represent asymmetric and symmetric COO^- stretching modes, respectively.[16] The peak at 1200 cm^{-1} is characteristic of C–N stretching vibrations.[17] A stretching vibration absorption band of C–O was also observed at 1095 cm^{-1}. FT-IR analysis of the prepared CDs confirmed the existence of hydroxy, carboxyl/carbonyl and nitrogen functional moieties. Fluorescence emission spectra of the CD solution were acquired across a range of excitation wavelengths (340–390 nm) (Fig. 1F). The CDs exhibited excitation-dependent emission characteristics, which was in line with previous research.[18] A systematic red-shift in emission maxima was observed with increasing excitation wavelength from 340 to 390 nm. This phenomenon, as previously documented, was a typical trait of CDs.[19,20] As displayed in Fig. 1G, the XPS full spectrum of CDs exhibited three major peaks assigned to C1s, N1s and O1s, confirming carbon, oxygen and nitrogen as the primary elemental components. The C1s spectrum showed four peaks at 287.6, 286.2, 285.5, 284.7 and 284.1 eV, which corresponded to C=O, C–N, C–O, C–C/C–H and C=C respectively.[21] The N1s spectrum showed two peaks at 400.0 and 399.3 eV, which assigned to N–$(C)_3$ and C=C–N groups.[22,23] In the O1s spectrum, the two peaks at 532.5 and 533.5 eV were assigned to C–OH/C–O–C and C=O, respectively. The combined XPS and FTIR

analyses validated that CDs possessed multiple surface functional groups, including hydroxyl, carboxyl and nitrogen moieties, a feature contributing to their superior hydrophilic properties.

When excited at 367 nm (Fig. 2A), CDs, DOX, and CDs–DOX exhibited distinct photoluminescence (PL) intensities. Specifically, CDs emitted a strong PL signal, while the fluorescence quenching of CDs–DOX was obvious, which further showed that there may be π–π conjugation between CDs and DOX. Meanwhile, CDs–DOX exhibited a blue shift relative to DOX, confirming the complexation.[24] As depicted in the UV-Vis absorption spectra of Fig. 2B, DOX had maximum peak at 490 nm. When DOX was loaded on CDs, the absorption peak of DOX at 490 nm shifted to the short wavelength direction, further validating their successful formation. As a typical spectral behavior of CDs–DOX systems, this blue-shift has been extensively described in earlier reports.[24] In Fig. 2C, the FT-IR spectra of CDs, DOX, and CDs–DOX are displayed in superposition. For the CDs, the absorption peaks indicate the presence of hydroxy, carboxyl/carbonyl and nitrogen functional groups. These functional groups endow CDs with hydrophilicity. Notably, the abundance of such functional groups highlights the structural flexibility of CDs, which is critical for DOX conjugation *via* electrostatic interactions. It could be seen from the FT-IR spectrum that CDs–DOX exhibited an additional characteristic peak of DOX compared with CDs, which further validated the successful formation of CDs–DOX. In this study, the drug-loading efficiency of DOX and *in vitro* release profile were systematically analyzed. Under the optimized conditions, it was found that the drug encapsulation efficiency (EE) was approximately 66.4%. Meanwhile, the drug loading

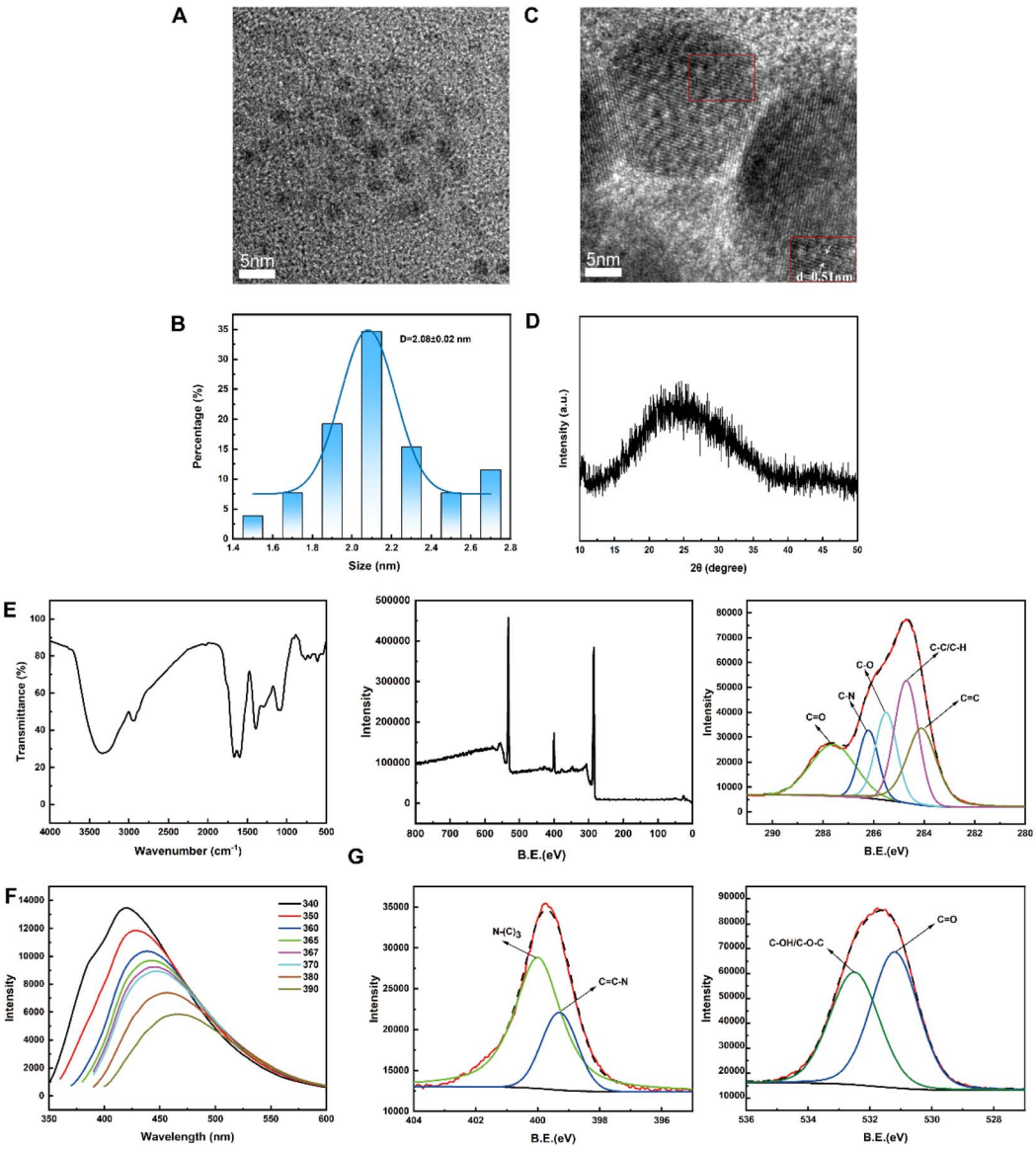

Fig. 1 Characterization of the CDs. (A) Representative TEM images of CDs. (B) Corresponding size distribution of CDs. (C) HRTEM images of CDs to show the crystal lattice. (D) XRD pattern of CDs. (E) FT-IR spectra of CDs. (F) Fluorescence emission profiles of CDs. (G) The survey scan and high-resolution C1s, N1s and O1s spectra obtained from XPS characterization of CDs.

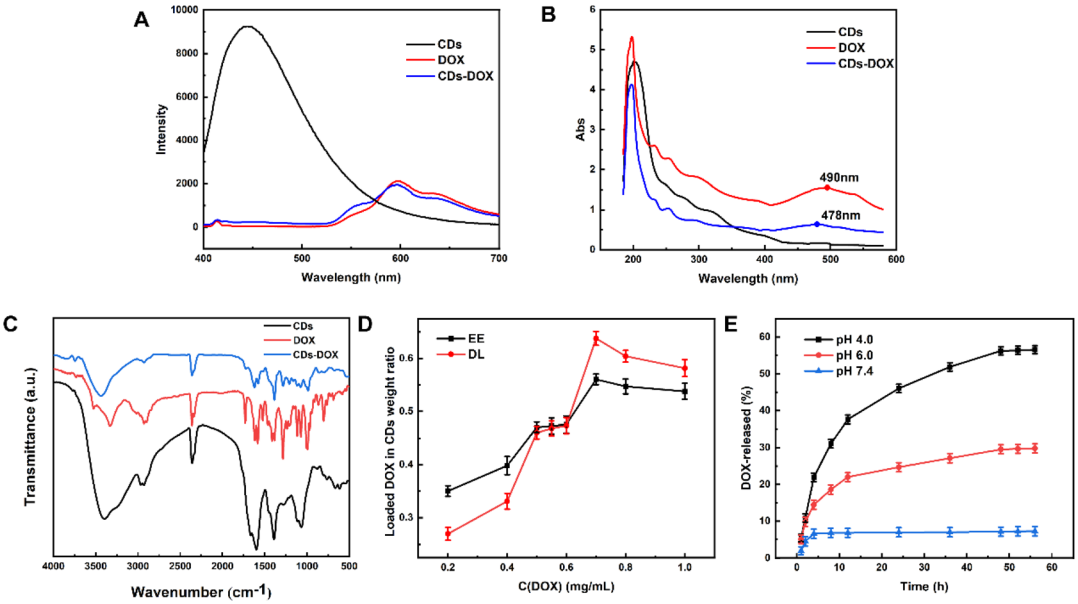

Fig. 2 Comprehensive analysis of CDs, DOX, and their conjugates including EE, DL, and release profiles. (A) Photoluminescence emission spectra of CDs, DOX, and CDs–DOX acquired. (B) UV-Vis absorption spectra of CDs solution, DOX aqueous solution, and CDs–DOX complex. (C) FT-IR spectra of CDs, DOX and CDs–DOX. (D)The EE and DL of DOX by the CDs. (E) DOX release from CDs was evaluated in PBS buffers at three pH values.

efficiency (DL) reached about 57.1% in Fig. 2D. The drug release performance of CDs–DOX in different pH PBS solutions was evaluated. The pH values of 4.0, 6.0, and 7.4 simulated the lysosomal environment within tumor cells, the endosomal environment, and normal physiological conditions, respectively. The release rate curves of CDs–DOX at different pH values are shown in Fig. 2E. Evidently, CDs–DOX demonstrated a significantly higher release rate in an acidic medium at pH 4.0 compared to pH 6.0 and 7.4. At pH 4.0, the cumulative release of CDs–DOX reached 56.55% after 56 h. However, at pH 7.4, it only reached 6.81%, indicating that the release rate of CDs–DOX was obviously pH-dependent, which proved that CDs–DOX could maintain a stable state in body fluids, and then slowly release the drug after DOX is transported into lysosomes in tumor cells. The pH-dependent of CDs–DOX was presumably attributed to the following: There were a large number of functional groups on the surface of CDs, such as hydroxy, carboxyl/carbonyl and nitrogen functional groups. These functional groups make CDs hydrophilic, and their protonated or deprotonated states change under different pH conditions. For example, in acidic environments (such as pH 5.0 in cancer cells), the degree of protonation of functional groups increases, affecting the stability of CD–DOX complexes; in neutral environments (such as normal physiological environment pH 7.4), the state of functional groups is different, and the complex is relatively more stable, resulting in decreased DOX release.[17] Therefore, CDs can transport DOX into tumor cells and enable sustained drug release.

3.2. CDs–DOX-L inhibited the growth of HCC

The subcutaneous transplantation tumor model of Hepa1-6 was constructed, and 1×10^7 Hepa1-6 cells were inoculated subcutaneously into the right hind limb of C57BL/6 mice (Fig. 3A). After 7 days tumor establishment, randomized grouping included PBS, CDs, CDs–DOX-L, CDs–DOX-M, CDs–DOX-H and DOX controls. There was no difference in body weight between the groups (Fig. 3B). The tumor growth in the PBS and CDs group was rapid, the tumor volume growth in the CDs–DOX-L, CDs–DOX-M, CDs–DOX-H and DOX groups was slowed down (Fig. 3C) ($P < 0.05$), and a significant suppression of tumor progression was observed. The tumor volume of the CDs–DOX-L group (21.91 $mm^3 \pm 3.256$ mm^3) was smaller than that of the PBS group (103.4 $mm^3 \pm 112.1$ mm^3) and the CDs group (326.5 $mm^3 \pm 195.3$ mm^3), indicating that CDs–DOX-L inhibited tumor growth. In addition, the tumor volume of the CDs–DOX-L (21.91 $mm^3 \pm 3.256$ mm^3) was 0.26 times that of the DOX group (85.16 $mm^3 \pm 47.11$ mm^3), indicating that the CDs–DOX-L group could better inhibit tumor growth (Fig. 3D). The results of this study showed that the anti-tumor effect of CDs–DOX did not show a dose-dependent relationship. The results of tumor weight showed that there was no difference between CDs–DOX-L, CDs–DOX-M, and CDs–DOX-H indicating no dose dependence, but there was a difference compared with CDs, indicating that CDs–DOX-L, CDs–DOX-M, and CDs–DOX-H could reduce the tumor weight (Fig. 3E). From the H&E staining of the tumor mass (Fig. 3F), it can be seen that the PBS and CDs group showed dense arrangement of tumor cells, abnormal morphology, and active tumor growth. The H&E staining of the CDs–DOX-L, CDs–DOX-M, and CDs–DOX-H groups showed relatively sparse arrangement of tumor cells and reduced morphological abnormalities. H&E staining of the DOX group showed that the tumor cells were relatively irregular. The expression level of Ki-67 is directly related to the

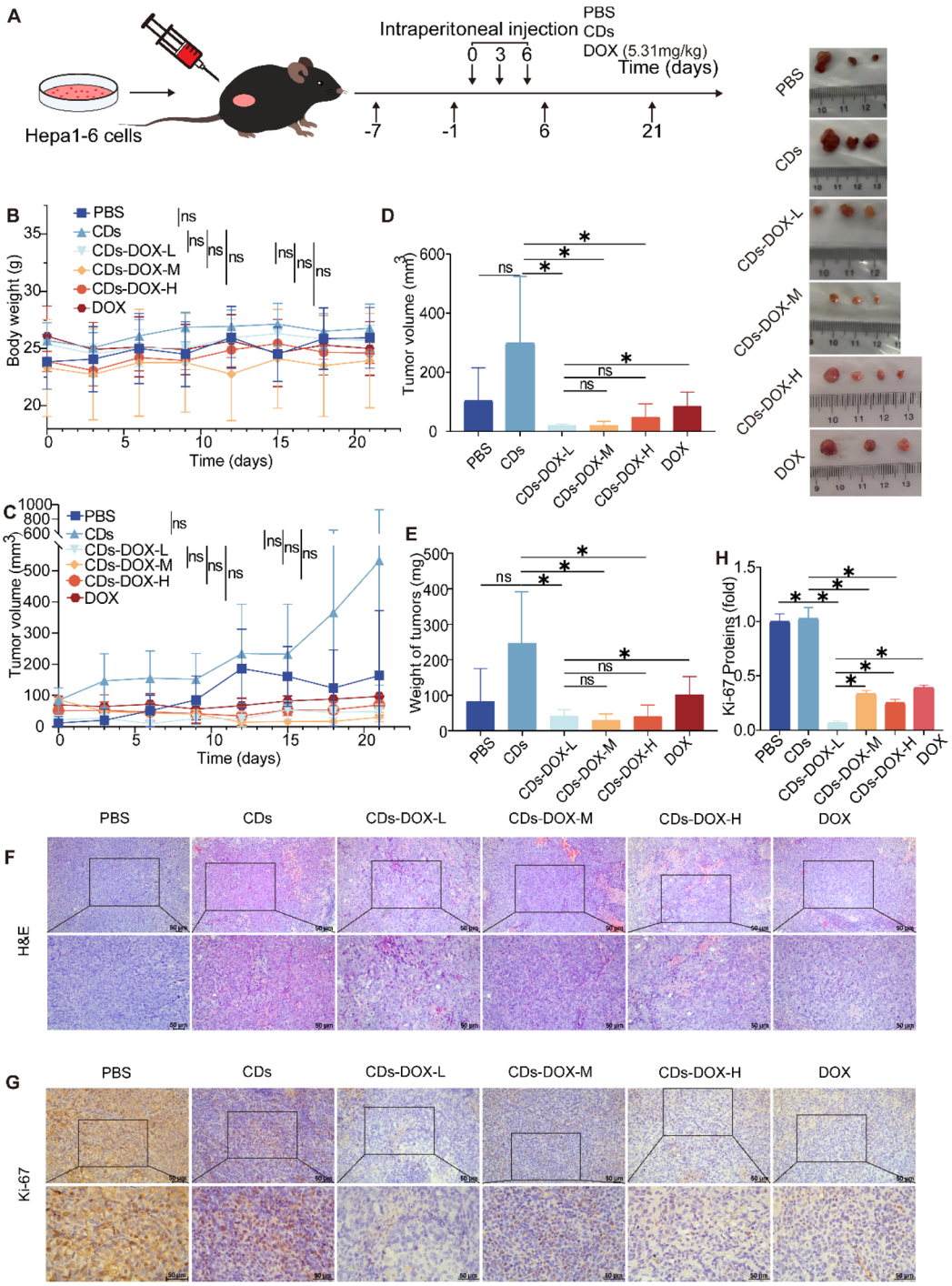

Fig. 3 The CDs–DOX demonstrated dual functionality by significantly suppressing Ki-67 proliferative marker expression and impeding subcutaneous tumor progression in murine models. (A) The schematic diagram describes the subcutaneous xenograft model of Hepa1-6 mice. (B) Changes of tumor volume in mice. (C) Changes in body weight of mice. (D) Tumor volume map of mice. (E) Tumor weight map of mice. (F) Tumor histopathology was observed by H&E staining (scale: 50 μm). (G) The positive expression of Ki-67 in mouse tumor cells was detected by immunohistochemical staining (scale: 50 μm). (H) Ki-67 quantitative analysis (*$P < 0.05$, ns $P > 0.05$, $n = 3$).

proliferation and expansion rate of tumor cells. Specifically, Ki-67 labeling index served as a reliable indicator of tumor aggressiveness, with higher indices predicting more rapid cellular proliferation.[25] IHC staining was conducted to quantify Ki-67-positive cells in tumor sections, providing a standardized measure of cellular proliferation. From the immunohistochemical staining of the tumor mass, the significant down-regulation of Ki-67 expression in the CDs–DOX-L group compared to CDs and DOX groups provides compelling evidence for its tumor growth-inhibiting properties (Fig. 3G and

H). This result is consistent with the data of tumor volume measurement, which further supports that CDs–DOX can inhibit tumor growth. And CDs–DOX-L has the best anti-tumor effect.

3.3. CDs–DOX-L increased the content of *A. muciniphila*

Previous studies have demonstrated the microbiota-modulating effects of *Artemisia argyi* in murine models. Building upon these findings, we utilized this medicinal herb as the precursor material for CDs synthesis.[26] To elucidate the microbiota-modulating effects of different treatments, fecal samples from PBS, CDs, and CDs–DOX-L-treated mice were subjected to 16 s rRNA gene sequencing analysis. The saturation of rarefaction curves with increasing sequencing depth indicated adequate coverage of microbial diversity in the samples. This feature indicates that the current sequencing depth is sufficient and the obtained data has high reliability (Fig. 4A).[27] Beta diversity analysis *via* PCoA revealed significant separation of intestinal microbiota profiles between treatment groups. Statistical analysis revealed significant intergroup variations, indicating that distinct therapeutic approaches exerted differential impacts on murine gut microbiota composition (Fig. 4B). A comprehensive evaluation of microbial diversity was conducted using established ecological indices, this study estimated a variety of alpha diversity indices, including Chao1, Goods-coverage, Simpson 's Index and Shannon–Wiener Index (Fig. 4C). The Simpson diversity index represents a widely employed ecological metric for quantifying microbial community heterogeneity within biological specimens. Comparative analysis showed marked differences in Simpson index values among treatment groups, reflecting substantial heterogeneity in microbial community structures. ($P < 0.05$).

At the same time, the phylum level diagram (Fig. 4D) and genus level diagram (Fig. 4E) were drawn, and the results clearly showed that there were some differences in the flora structure of each sample. The relative abundance ratio of Firmicutes *versus* Bacteroidetes (F/B) was computed to evaluate treatment-induced alterations in intestinal microbial architecture. Compared with PBS group and CDs group, the F/B ratio of CDs–DOX-L group increased, indicating that CDs–DOX-L changed the intestinal flora of mice. Heatmap analysis of species composition revealed distinct clustering patterns, highlighting potential microbial biomarkers characteristic of each treatment group. It was found that the content of *A. muciniphila* in PBS, CDs and CDs–DOX-L groups increased gradually, and the number of CDs–DOX-L group was the highest (Fig. 4F). As a probiotic bacterium, *A. muciniphila* contributes to intestinal homeostasis through its ability to modulate mucus barrier dynamics and maintain microbial community stability.[28–31] Experimental data demonstrate that the CDs–DOX-L formulation exhibits dual therapeutic benefits: potent antitumor efficacy coupled with favorable modulation of gut microbial communities. This study further extracted the fecal DNA of mice in PBS, CDs, and CDs–DOX-L groups, and performed PCR detection of *A. muciniphila.* Consistent with the results of 16 s r RNA sequencing, CDs–DOX-L has a good ability to reshape the composition of intestinal flora in tumor-bearing mice (Fig. 4G), which further confirmed the reliability of the research conclusions.

3.4. CDs–DOX-L improved intestinal barrier

Following characterization of microbiota alterations, intestinal histopathological evaluation was conducted through H&E and PAS staining to assess drug-induced morphological changes and mucosal barrier integrity. The results of H&E staining showed that the colon tissue structure of mice in each group was intact, and no obvious pathological damage was observed, indicating that no significant detrimental impact on intestinal architecture was observed in drug-treated mice (Fig. 5A). PAS staining revealed a marked increase in goblet cell density within colonic tissues of the CDs–DOX-L treatment group (Fig. 5B). The increase in the number of goblet cells is usually regarded as an important indicator of the improvement of intestinal barrier function.[32] ZO-1, belonging to the MAGUK protein family, plays a pivotal role in cellular organization by serving as a scaffold that binds and stabilizes transmembrane proteins. It connects tight junction complexes to cortical actin, maintaining epithelial junction stability.[33] Merging evidence indicates that reduced ZO-1 expression correlates with enhanced tumor dissemination and metastatic progression.[34] As a critical tight junction component, Occludin serves as a primary regulator of intestinal barrier dysfunction in various pathological conditions.[35] The CDs–DOX-L group exhibited upregulated ZO-1 and Occludin expression, indicating improved intestinal barrier integrity (Fig. 5C and D).[36,37]

3.5. CDs–DOX-L regulated genes and pathways in tumor cells

After sample processing, RNA sequencing bioinformatics analysis was performed to preliminarily explore the related biological changes after CDs–DOX-L treatment. Pearson correlation coefficients were calculated to evaluate the association between continuous variables and assess similarity in gene expression profiles across samples. A stronger positive correlation (closer to 1) reflects greater similarity in expression patterns. As shown in the figure, the correlation between samples is higher, and the heat map shows that there is a positive correlation between all samples (Fig. 6A). Principal component analysis uncovered markedly differentiated transcriptomic profiles across study groups (Fig. 6B). The overall distribution of DEG can be inferred from the volcanic map. Comparative analysis of DEGs demonstrated significant variations in gene expression patterns when comparing CDs and CDs–DOX-L groups. A total of 135 genes ($|\log 2FC = > 1$ and $P < 0.05$) were detected, including 63 up-regulated and 72 down-regulated genes. After CDs–DOX-L treatment, 135 genes were up-regulated, indicating a significant regulatory effect on cell gene expression.[38]

In the volcano map, we found that the following genes are closely related to HCC (Fig. 6C). *ISG15* is a novel prognostic marker for predicting 5 year overall survival in patients with HBV-related HCC. The overexpression of *ISG15* is associated with clinicopathological features and poor prognosis of patients.[39] The article proposes that patients with higher *NPAS2*

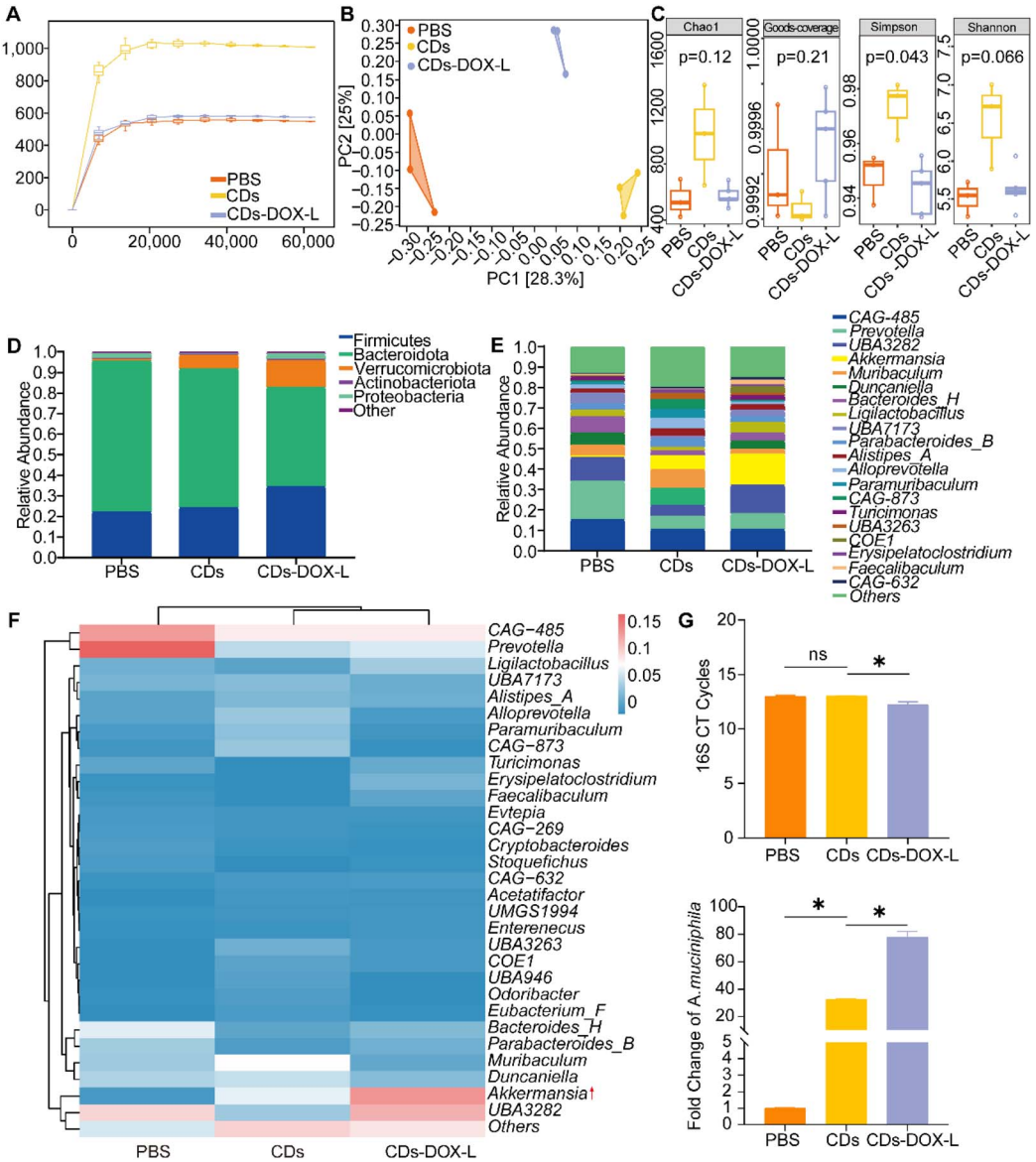

Fig. 4 CDs–DOX improved the intestinal flora of mice and increased the content of *A. muciniphila*. (A) Sparse curves of 16 s rRNA gene sequencing in different groups of mice. (B) PCoA maps of different groups of mice. (C) The alpha diversity indices of mice from different groups. (D) Taxonomic composition distribution at the phylum level. (E) Distribution of species taxonomic composition at the genus level. (F) Showed the heat map of the top 20 species in the species composition of each group of mice. (G) Real-time fluorescence quantitative PCR was used to detect the total number of bacteria and *A. muciniphila* in different groups (*$P < 0.05$, ns $P > 0.05$, $n = 3$).

expression have a poor prognosis.[40] Based on the predicted target genes, their molecular functions were further analyzed. *SAMD12* may play an alternating role in postoperative effects and tumor size, which may lead to carcinogenesis.[41] The experiment confirmed the cancer-promoting function of *RSPO3* and its regulation on immune infiltration.[42] Ces enzymes (*Ces1d*, *Ces1f*, *Ces3b*), which are important regulators of VLDL lipid packaging and assembly in the endoplasmic reticulum (ER) of the liver, reduce their expression will lead to reduced liver lipid clearance.[43] The significant up-regulation (*Ces1d*) or down-regulation (*ISG15*, *NPAS2*, *SAMD12*, *RSPO3*) of these genes exert anti-tumor immune effects, thereby inhibiting the occurrence and development of cancer.

Functional annotation of genes with significant changes in CDs–DOX-L was performed by GO and KEGG pathway enrichment analysis (Fig. 6D and E). GO term analysis found that CDs–DOX treatment may enhance the anti-tumor immune response by participating in NK cell-mediated killing and triggering inflammatory cell death. KEGG enrichment analysis showed that CDs–DOX may activate chemokine-mediated immune cell recruitment, synergistic anti-tumor effect of Wnt/calcium signaling pathway, regulate tumor microenvironment and metabolic recombination, and form a multi-level immune-enhancing anti-tumor mechanism. Cluster analysis was employed to identify distinct expression patterns of differentially expressed genes (DEGs) across experimental conditions

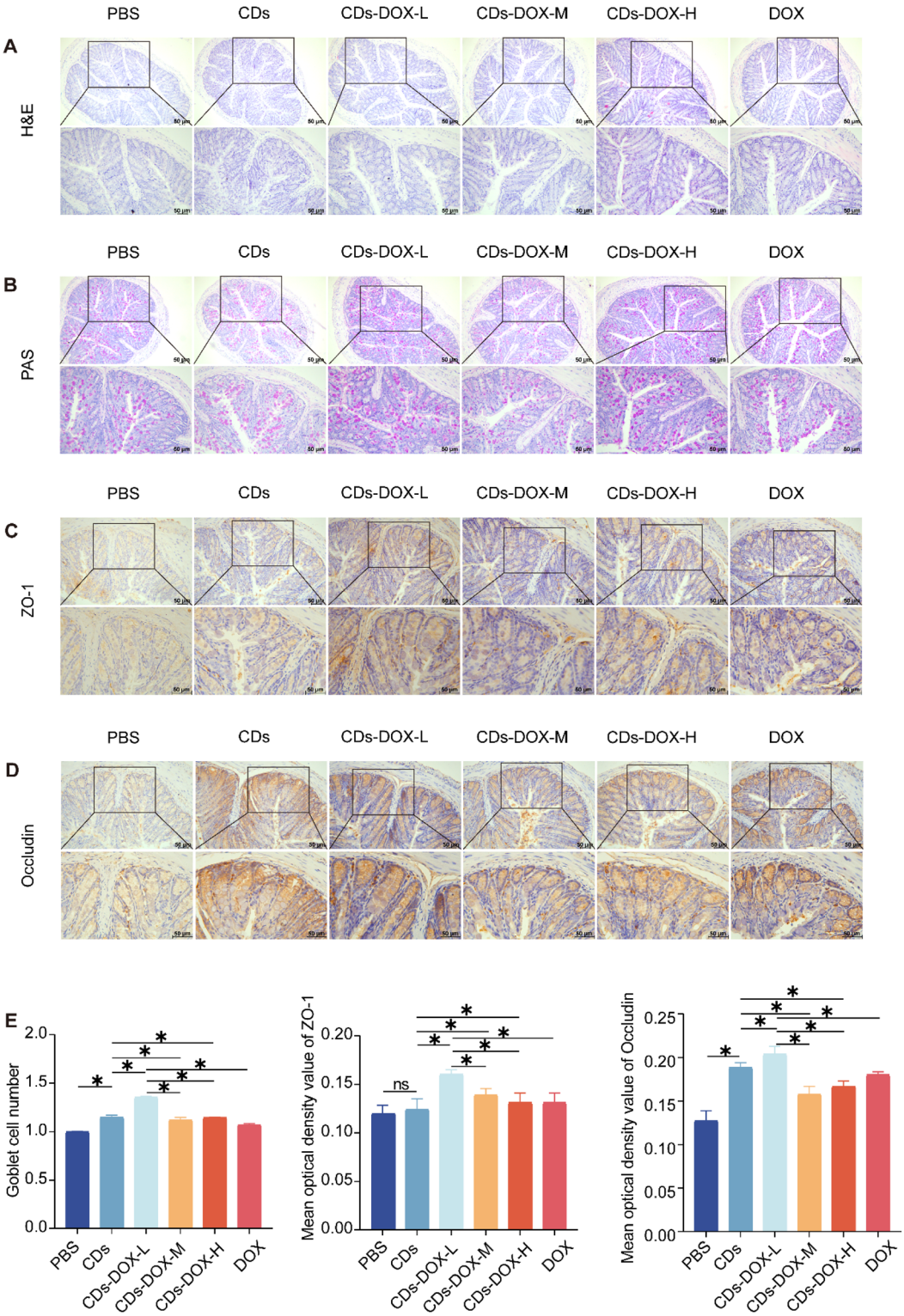

Fig. 5 CDs–DOX administration demonstrated protective effects on the intestinal barrier in mice, showing significant increases in both goblet cell density and the protein levels of ZO-1 and Occludin. (A) Colon tissue morphology was assessed through conventional H&E staining protocols (scale: 50 μm). (B) PAS staining was employed to quantify goblet cell within mice colonic tissues (scale: 50 μm) (C) Immunohistochemical staining (scale: 50 μm) was performed to assess ZO-1 protein expression patterns. (D) Immunohistochemical staining (ruler: 50 μm) was used to observe the positive expression of Occludin. (E) Goblet cell quantification and expression levels of ZO-1 and Occludin were assessed. (*$P < 0.05$, ns $P > 0.05$, $n = 3$).

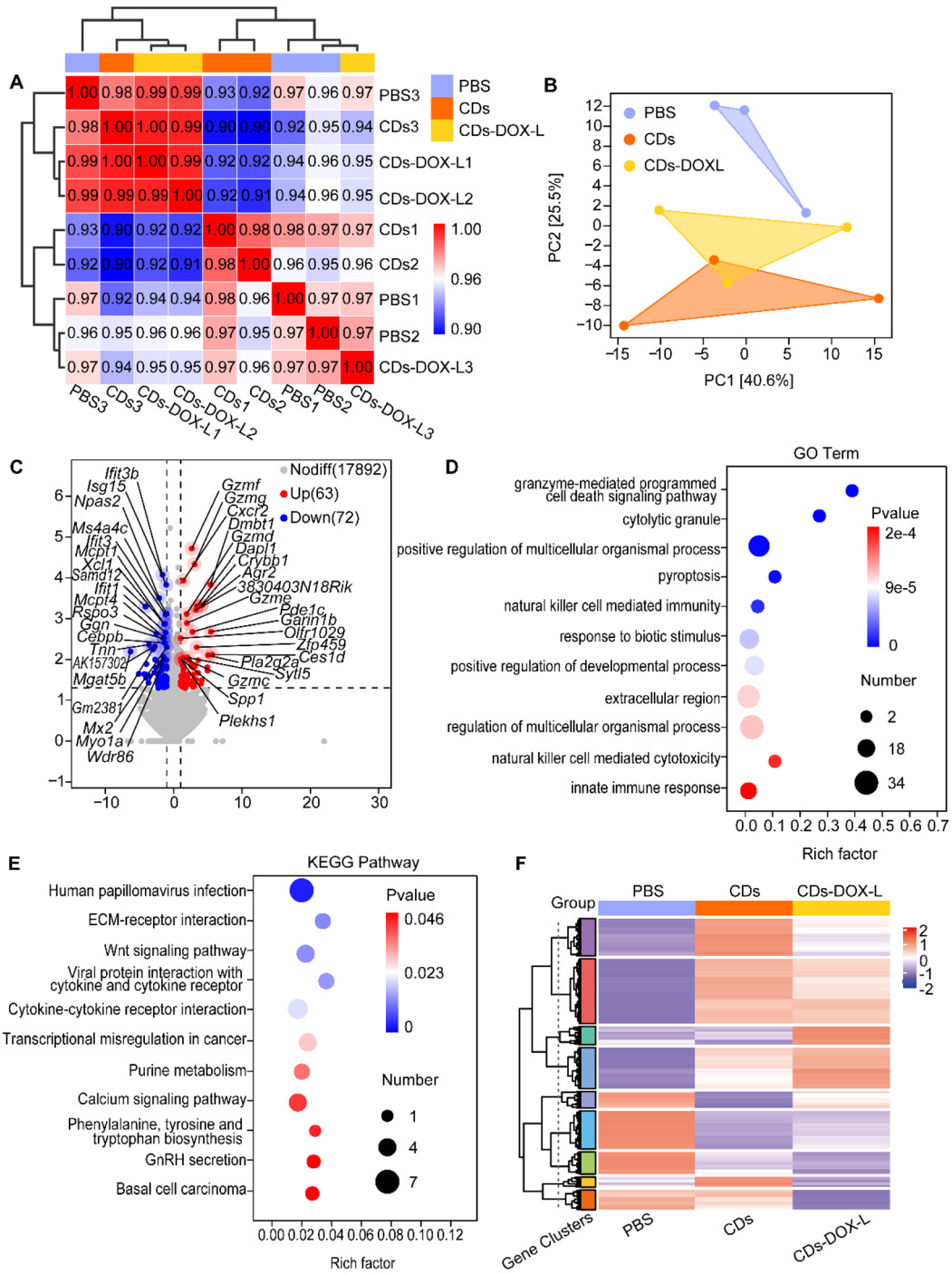

Fig. 6 Transcriptome sequencing analysis of PBS, CDs and CDs–DOX-L groups. (A) Gene expression profile similarity between samples was quantified using Pearson correlation coefficients, where values approaching 1 indicate higher degrees of transcriptional pattern concordance. (B) In the PCA plot, distinct sample groups are differentiated by both geometric shapes and color coding. (C) Volcano map of DEGs. The gene of red dots was up-regulated, the gene of blue dots was down-regulated, and the gene difference of gray dots was not significant. (D) GO enrichment analysis. (E) KEGG enrichment analysis. (F) Cluster analysis (*$P < 0.05$, $n = 3$).

(Fig. 6F). CDs–DOX-L inhibits the expression of HCC-related genes and exerts anti-tumor effects by regulating up-regulated genes (*Ces1d*) and down-regulated genes (*ISG15*, *NPAS2*, *SAMD12*, *RSPO3*) and immune-related pathways.

3.6. CDs–DOX reduced the heart and liver toxicity

H&E staining was used to detect the internal organs of HCC mice treated with different drugs (Fig. 7A–E). To evaluate drug toxicity *in vivo*, we collected the heart, liver, spleen, lungs, and kidneys from mice and prepared them for histological analysis.

The anthracycline antibiotic DOX represents a widely utilized chemotherapeutic drug with activity against multiple cancer types. While DOX is clinically effective, its utility is constrained by progressive cardiac damage. The toxic effects of DOX lead to muscle cell damage, eventually leading to pathological cardiomyopathy.[44,45] Myocardial injury was found in DOX heart tissue sections, and no obvious injury was found in other groups (Fig. 7A). In addition, studies indicate that DOX induces hepatotoxicity[46,47] while the liver tissue of the CDs–DOX was less damaged, reducing the toxic and side effects of DOX (Fig. 7B). The CDs–DOX exhibits markedly lower toxicity profiles in both heart and liver tissues, compared to DOX. A marked increase in

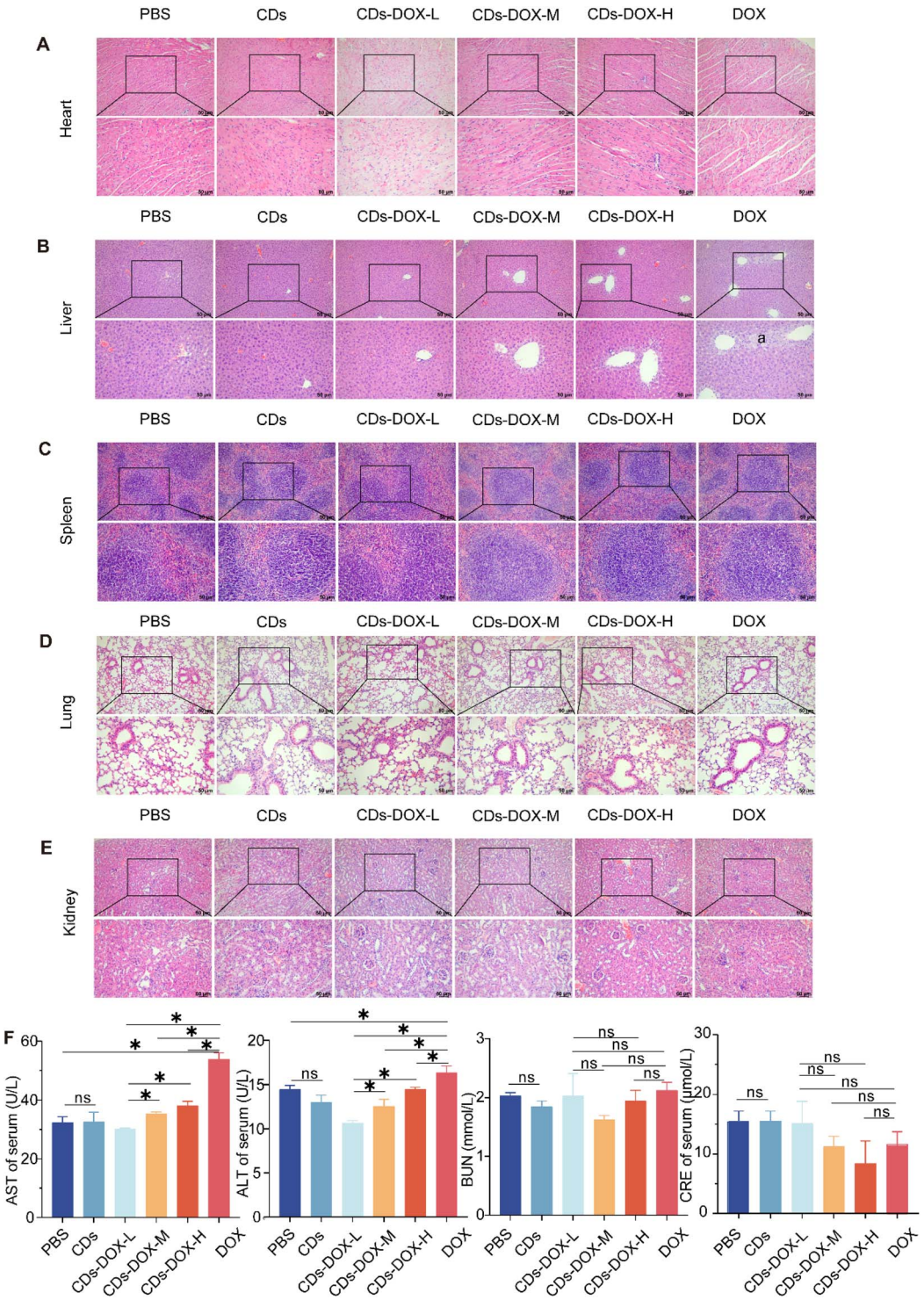

Fig. 7 CDs–DOX reduced the hepatotoxicity of the drug. (A–E) H&E staining (scale: 50 μm) was used to observe the histopathology of heart, liver, spleen, lung and kidney in mice. (F) Detection of AST, ALT, BUN and CRE in serum of mice. (*$P < 0.05$, ns $P > 0.05$, $n = 3$).

AST levels was observed in DOX-treated mice relative to PBS controls ($P < 0.05$), confirming DOX hepatotoxic potential. Comparative analysis revealed statistically significant differences between CDs–DOX and DOX treatment groups ($P < 0.05$), and the AST value of the CDs–DOX was significantly reduced, which strongly proved that the CDs–DOX can effectively reduce the toxic effects of DOX on the liver of mice. CDs–DOX-L had significantly less liver damage, suggesting that it could more effectively reduce liver side effects, compared with CDs–DOX-M and CDs–DOX-H. Similarly, the analysis results of ALT indicators further confirmed that the CDs–DOX had a significant improvement effect on DOX-induced liver toxicity (Fig. 7F). In addition, through the evaluation of BUN and CRE indicators, statistical analysis revealed no treatment effect relative to controls ($P > 0.05$) (Fig. 7F). The above experiments fully proved that CDs–DOX reduced drug heart and liver toxicity and provided an important basis for clinical safe medication.

4 Conclusion

In conclusion, this study demonstrates for the first time that hydrothermal treatment of *Artemisia argyi* represents an efficient approach for synthesizing carbon dots. The CDs displayed a uniform quasi-spherical shape (~2 nm diameter) with surface hydroxyl, carboxyl, and methyl groups, contributing to their excellent hydrophilicity. Successful fabrication of the CDs–DOX was confirmed by PL, UV-Vis, and FT-IR spectroscopy, which showed significant variations compared to pristine CDs. The CDs–DOX show minimal drug release in pH 6.0 and pH 7.4, while release drugs rapidly and quantitatively in acidic environment (pH 4.0), which exhibited pH-dependent DOX release properties. The results of animal experiments showed that CDs–DOX-L reduced the expression of Ki-67 and effectively inhibited tumor growth. In addition, CDs–DOX-L significantly increased the content of *A. muciniphila*, optimized the structure of intestinal flora in mice, and improved the intestinal barrier. Transcriptomic profiling revealed critical regulatory genes and oncogenic pathways implicated in hepatocellular carcinoma therapeutics. It is worth noting that CDs–DOX significantly reduces the heart and liver toxicity of DOX and provides a safer and more efficient innovative solution for tumor treatment. These research results show that CDs–DOX has better clinical transformation application prospects.

Ethical statement

The study was evaluated and approved by the Animal Experiment Ethics Committee of Shanxi University of Chinese Medicine, with the approval number AWE202403287.

Author contributions

Ruilong Jia: Writing-review & editing, supervision, formal analysis. Ping Liu: Writing–original draft, investigation, formal analysis. Yanli Gong: Data curation. Yuting Gao: Methodology. Yajun Xiong: Investigation. Xiaoyong Song: Investigation. Jinglin Peng: Data curation. Meiqi Lan: Investigation. Xinli Shi: Writing-review & editing, supervision, funding acquisition, conceptualization.

Conflicts of interest

The authors assert having no known competing financial interests or personal relationships likely to influence the work detailed in this paper.

Data availability

The datasets produced and analyzed in this study can be obtained from the corresponding author upon reasonable request.

Acknowledgements

This work was supported by the Basic Research Planned Project of Shanxi Provincial Department of Science and Technology (Grant No. 202203021212338), the Shanxi Provincial Administration of Traditional Chinese Medicine Innovation Team (Grant No. zyytd2024021), the Key Research Office of Shanxi Province Administration of Traditional Chinese Medicine (zyyyjs2024035), and the Foundation for High-level Talents of Shanxi University of Chinese Medicine (2023RC03). The Open Fund of Shanxi Key Laboratory of Innovative Drug for the Treatment of Serious Diseases Basing on the Chronic Inflammation, Shanxi University of Chinese Medicine. Fund for the Discipline of Chinese Materia Medica Pharmaceutics, Shanxi University of Chinese Medicine (2025XK35).

References

1 H. Sung, J. Ferlay, R. L. Siegel, M. Laversanne, I. Soerjomataram, A. Jemal and F. Bray, Global Cancer Statistics 2020: GLOBOCAN Estimates of Incidence and Mortality Worldwide for 36 Cancers in 185 Countries, *CA-Cancer J. Clin.*, 2021, **71**, 209–249.
2 J. S. Du, S. H. Hsu and S. N. Wang, The Current and Prospective Adjuvant Therapies for Hepatocellular Carcinoma, *Cancers*, 2024, **16**, 1422–1436.
3 L. Rajendran, T. Ivanics, M. P. Claasen, H. Muaddi and G. Sapisochin, The management of post-transplantation recurrence of hepatocellular carcinoma, *Clin. Mol. Hepatol.*, 2022, **28**, 1–16.
4 J. Wang, Q. Liu, Y. Zhao, J. Fu and J. Su, Tumor Cells Transmit Drug Resistance *via* Cisplatin-Induced Extracellular Vesicles, *Int. J. Mol. Sci.*, 2023, **24**, 12347–12365.
5 C. M. Tilsed, S. A. Fisher, A. K. Nowak, R. A. Lake and W. J. Lesterhuis, Cancer chemotherapy: insights into cellular and tumor microenvironmental mechanisms of action, *Front. Oncol.*, 2022, **12**, 960317–960334.
6 P. K. Dhanyamraju, T. D. Schell, S. Amin and G. P. Robertson, Drug-Tolerant Persister Cells in Cancer Therapy Resistance, *Cancer Res.*, 2022, **82**, 2503–2514.
7 Y. Li, J. Yan and P. Yang, The mechanism and therapeutic strategies in doxorubicin-induced cardiotoxicity: Role of

programmed cell death, *Cell Stress Chaperones*, 2024, **29**, 666–680.

8 R. Mattioli, A. Ilari, B. Colotti, L. Mosca, F. Fazi and G. Colotti, Doxorubicin and other anthracyclines in cancers: Activity, chemoresistance and its overcoming, *Mol. Aspects Med.*, 2023, **93**, 101205–101247.

9 A. Ansary, A. Osman and M. E. El-Khouly, Doxorubicin-loaded pH-responsive porphyrin-derived carbon dots as a promising biocompatible drug delivery system for effective chemotherapy of breast cancer, *RSC Adv.*, 2025, **15**, 6457–6473.

10 C. Wang, J. Li, K. Liu, J. Li, F. Zhang, X. Ma, Y. Li, C. Zhang, X. Liu, Y. Qu, M. Zhao, W. Li, W. Huang and Y. Q. Li, Donkey-Hide Gelatin-Derived Carbon Dots Activate Erythropoiesis and Eliminate Oxidative Stress for Aplastic Anemia Treatment, *ACS Nano*, 2025, **19**, 2922–2935.

11 Z. Deng, Y. Zhang, R. Li, Y. Zhu, C. Xu, B. Gao, W. Wang, C. Ding, B. He and X. J. Zhu, Honeysuckle-Derived Carbon Dots With Robust Catalytic and Pharmacological Activities for Mitigating Lung Inflammation by Inhibition of Caspase11/GSDMD-Dependent Pyroptosis, *Adv. Funct. Mater.*, 2025, **35**, 2418683–2418701.

12 D. Li, K. Y. Xu, W. P. Zhao, M. F. Liu, R. Feng, D. Q. Li, J. Bai and W. L. Du, Chinese Medicinal Herb-Derived Carbon Dots for Common Diseases: Efficacies and Potential Mechanisms, *Front. Pharmacol.*, 2022, **13**, 815479–815488.

13 H. Zhang, Z. Hao, R. Zhang, J. Tong, X. Wang, J. Liu, Y. Gao, X. Wang, Q. Su, H. Wen, Y. Fan, F. Liu, X. Li, C. Tong and X. Wang, Artemisia argyi polyphenols Attenuates DSS-induced colitis in mice by regulating the structural composition of gut microbiota, *Phytomedicine*, 2024, **132**, 155897–155911.

14 Y. Yang, Y. Gao, Y. Gong, J. Lu, S. Li, Y. Xiong, Y. Zhang, D. Wang, P. Gong, Y. Li and X. Shi, Dihydroartemisinin breaks the immunosuppressive tumor niche during cisplatin treatment in Hepatocellular carcinoma, *Acta Histochem.*, 2024, **126**, 152171–152179.

15 J. Lu, Y. Gong, Y. Gao, Y. Yang, Y. Zhang, Z. Zhang and X. Shi, Wolfberry, Yam, and Chrysanthemum polysaccharides increased intestinal Akkermansia muciniphila abundance and hepatic YAP1 expression to alleviate DILI, *FASEB*, 2023, **37**, e23286–e23300.

16 M. J. Bojdys, J.-O. Müller, M. Antonietti and A. Thomas, Ionothermal Synthesis of Crystalline, Condensed, Graphitic Carbon Nitride, *Chem.–Eur. J*, 2008, **14**, 8177–8182.

17 Y. Yuan, B. Guo, L. Hao, N. Liu, Y. Lin, W. Guo, X. Li and B. Gu, Doxorubicin-loaded environmentally friendly carbon dots as a novel drug delivery system for nucleus targeted cancer therapy, *Colloids Surf., B*, 2017, **159**, 349–359.

18 J. Hou, J. Yan, Q. Zhao, Y. Li, H. Ding and L. J. N. Ding, A novel one-pot route for large-scale preparation of highly photoluminescent carbon quantum dots powders, *Nanoscale*, 2013, **5**, 9558–9561.

19 M. Jahanbakhshi and B. J. B. Habibi, Bioelectronics, A novel and facile synthesis of carbon quantum dots *via* salep hydrothermal treatment as the silver nanoparticles support: Application to electroanalytical determination of H2O2 in fetal bovine serum, *Biosens. Bioelectron.*, 2016, **81**, 143–150.

20 M. Algarra, B. B. Campos, K. Radotić, D. Mutavdžić, T. Bandosz, J. Jimenez-Jimenez, E. Rodriguez-Castellon and J. C. da Silva, Luminescent carbon nanoparticles: effects of chemical functionalization, and evaluation of Ag+ sensing properties, *J. Mater. Chem. A*, 2014, **2**, 8342–8351.

21 S. Liu, J. Tian, L. Wang, Y. Luo, J. Zhai and X. J. Sun, Preparation of photoluminescent carbon nitride dots from CCl4 and 1, 2-ethylenediamine: a heat-treatment-based strategy, *J. Mater. Chem. A*, 2011, **21**, 11726–11729.

22 K. Qu, J. Wang, J. Ren and X. Qu, Carbon dots prepared by hydrothermal treatment of dopamine as an effective fluorescent sensing platform for the label-free detection of iron(III) ions and dopamine, *Chemistry*, 2013, **19**, 7243–7249.

23 S. Lu, S. Guo, P. Xu, X. Li, Y. Zhao, W. Gu and M. Xue, Hydrothermal synthesis of nitrogen-doped carbon dots with real-time live-cell imaging and blood–brain barrier penetration capabilities, *Int. J. Nanomed.*, 2016, **11**, 6325–6336.

24 L. Yang, Z. Wang, J. Wang, W. Jiang, X. Jiang, Z. Bai, Y. He, J. Jiang, D. Wang and L. J. N. Yang, Doxorubicin conjugated functionalizable carbon dots for nucleus targeted delivery and enhanced therapeutic efficacy, *Nanoscale*, 2016, **8**, 6801–6809.

25 L. T. Li, G. Jiang, Q. Chen and J. N. Zheng, Ki67 is a promising molecular target in the diagnosis of cancer (review), *Mol. Med. Rep.*, 2015, **11**, 1566–1572.

26 Q. Ma, D. Tan, X. Gong, H. Ji, K. Wang, Q. Lei and G. Zhao, An Extract of Artemisia argyi Leaves Rich in Organic Acids and Flavonoids Promotes Growth in BALB/c Mice by Regulating Intestinal Flora, *Animals*, 2022, **12**, 1519–1535.

27 J. Lu, Y. Gao, Y. Gong, Y. Yue, Y. Yang, Y. Xiong, Y. Zhang, Y. Xiao, H. Wang, H. Fan and X. Shi, Lycium barbarum L. Balanced intestinal flora with YAP1/FXR activation in drug-induced liver injury, *Int. Immunopharmacol.*, 2024, **130**, 111762–111774.

28 J. Y. Yang, Y. S. Lee, Y. Kim, S. H. Lee, S. Ryu, S. Fukuda, K. Hase, C. S. Yang, H. S. Lim, M. S. Kim, H. M. Kim, S. H. Ahn, B. E. Kwon, H. J. Ko and M. N. Kweon, Gut commensal Bacteroides acidifaciens prevents obesity and improves insulin sensitivity in mice, *Mucosal Immunol.*, 2017, **10**, 104–116.

29 J. Chhimwal, P. Anand, P. Mehta, M. K. Swarnkar, V. Patial, R. Pandey and Y. Padwad, Metagenomic signatures reveal the key role of phloretin in amelioration of gut dysbiosis attributed to metabolic dysfunction-associated fatty liver disease by time-dependent modulation of gut microbiome, *Front. Microbiol.*, 2023, **14**, 1210517–1210534.

30 J. Xia, L. Lv, B. Liu, S. Wang, S. Zhang, Z. Wu, L. Yang, X. Bian, Q. Wang, K. Wang, A. Zhuge, S. Li, R. Yan, H. Jiang, K. Xu and L. Li, Akkermansia muciniphila Ameliorates Acetaminophen-Induced Liver Injury by Regulating Gut Microbial Composition and Metabolism, *Microbiol. Spectrum*, 2022, **10**, e0159621–e0159639.

31 K. Y. He, X. Y. Lei, D. H. Wu, L. Zhang, J. Q. Li, Q. T. Li, W. T. Yin, Z. L. Zhao, H. Liu, X. Y. Xiang, L. J. Zhu,

C. Y. Cui, K. K. Wang, J. H. Wang, L. Lv, Q. H. Sun, G. L. Liu, Z. X. Xu and Y. P. Jian, Akkermansia muciniphila protects the intestine from irradiation-induced injury by secretion of propionic acid, *Gut Microbes*, 2023, **15**, 2293312–2293334.

32 J. K. Gustafsson and M. E. V. Johansson, The role of goblet cells and mucus in intestinal homeostasis, *Nat. Rev. Gastroenterol. Hepatol.*, 2022, **19**, 785–803.

33 C. J. Gottardi, M. Arpin, A. S. Fanning and D. Louvard, The junction-associated protein, zonula occludens-1, localizes to the nucleus before the maturation and during the remodeling of cell-cell contacts, *Proc. Natl. Acad. Sci. U. S. A.*, 1996, **93**, 10779–10784.

34 Y. Gao, T. Luo, X. Ouyang, C. Zhu, J. Zhu and X. Qin, IGF2BP3 and miR191-5p synergistically increase HCC cell invasiveness by altering ZO-1 expression, *Oncol. Lett.*, 2020, **20**, 1423–1431.

35 T. Yumoto, T. Oami, Z. Liang, E. M. Burd, M. L. Ford, J. R. Turner and C. M. Coopersmith, INTESTINAL EPITHELIAL-SPECIFIC OCCLUDIN DELETION WORSENS GUT PERMEABILITY AND SURVIVAL FOLLOWING SEPSIS, *Shock*, 2025, **63**, 597–605.

36 W. T. Kuo, L. Zuo, M. A. Odenwald, S. Madha, G. Singh, C. B. Gurniak, C. Abraham and J. R. Turner, The Tight Junction Protein ZO-1 Is Dispensable for Barrier Function but Critical for Effective Mucosal Repair, *Gastroenterology*, 2021, **161**, 1924–1939.

37 K. Saha, A. Subramenium Ganapathy, A. Wang, N. Michael Morris, E. Suchanec, W. Ding, G. Yochum, W. Koltun, M. Nighot, T. Ma and P. Nighot, Autophagy Reduces the Degradation and Promotes Membrane Localization of Occludin to Enhance the Intestinal Epithelial Tight Junction Barrier against Paracellular Macromolecule Flux, *J. Crohn's Colitis*, 2023, **17**, 433–449.

38 Y. Gao, Y. Gong, Y. Liu, Y. Xue, K. Zheng, Y. Guo, L. Hao, Q. Peng and X. Shi, Integrated analysis of transcriptomics and metabolomics in human hepatocellular carcinoma HepG2215 cells after YAP1 knockdown, *Acta Histochem.*, 2023, **125**, 151987–151998.

39 X. Qiu, Y. Hong, D. Yang, M. Xia, H. Zhu, Q. Li, H. Xie, Q. Wu, C. Liu and C. Zuo, ISG15 as a novel prognostic biomarker for hepatitis B virus-related hepatocellular carcinoma, *Int. J. Clin. Exp. Med.*, 2015, **8**, 17140–17150.

40 Z. Zhang, Z. Liang, W. Gao, S. Yu, Z. Hou, K. Li and P. Zeng, Identification of circadian clock genes as regulators of immune infiltration in Hepatocellular Carcinoma, *J. Cancer*, 2022, **13**, 3199–3208.

41 J. Hu, C. Xie, S. Xu, Q. Pu, H. Liu, L. Yang, W. Wang, L. Mao, Z. Li and W. Chen, Liver fibrosis-derived exosomal miR-106a-5p facilitates the malignancy by targeting SAMD12 and CADM2 in hepatocellular carcinoma, *PLoS One*, 2023, **18**, e0286017–e0286031.

42 Q. Liu, H. Zhang, H. Xiao, A. Ren, Y. Cai, R. Liao, H. Yu, Z. Wu and Z. Huang, Discovery of novel diagnostic biomarkers of hepatocellular carcinoma associated with immune infiltration, *Ann. Med.*, 2025, **57**, 2503645–2503656.

43 M. J. Lyall, J. Cartier, J. A. Richards, D. Cobice, J. P. Thomson, R. R. Meehan, S. M. Anderton and A. J. Drake, Methyl donor deficient diets cause distinct alterations in lipid metabolism but are poorly representative of human NAFLD, *Wellcome Open Res.*, 2017, **2**, 67–85.

44 C. Y. Kong, Z. Guo, P. Song, X. Zhang, Y. P. Yuan, T. Teng, L. Yan and Q. Z. Tang, Underlying the Mechanisms of Doxorubicin-Induced Acute Cardiotoxicity: Oxidative Stress and Cell Death, *Int. J. Biol. Sci.*, 2022, **18**, 760–770.

45 N. Shelburne, N. I. Simonds, B. Adhikari, M. Alley, P. Desvigne-Nickens, E. Dimond, K. Filipski, L. Gallicchio and L. Minasian, Changing Hearts and Minds: Improving Outcomes in Cancer Treatment-Related Cardiotoxicity, *Curr. Oncol. Rep.*, 2019, **21**, 9–17.

46 E. Gedikli, V. Barış, N. Yersal, A. B. Dinçsoy, S. F. Müftüoğlu and A. Erdem, Taurine Protects Doxorubicin-Induced Hepatotoxicity *via* Its Membrane-Stabilizing Effect in Rats, *Life*, 2023, **13**, 2031–2043.

47 D. J. Marchand and K. W. Renton, Depression of cytochrome P-450-dependent drug biotransformation by adriamycin, *Toxicol. Appl. Pharmacol.*, 1981, **58**, 83–88.